

Towards accurate atom scale characterisation of hydrogen passivation of interfaces in TOPCon architectures

Yifu Shi^a, Megan E. Jones^a, Martin S. Meier^a, Matthew Wright^a, Jana-Isabelle Polzin^b,
Wolfram Kwapil^{b,c}, Christian Fischer^d, Martin C. Schubert^b, Chris Grovenor^a, Michael Moody^a,
Ruy S. Bonilla^{a,*}

^a Department of Materials, University of Oxford, Oxford, OX1 3PH, United Kingdom

^b Fraunhofer Institute for Solar Energy ISE, Heidenhofstr. 2, 79110, Freiburg, Germany

^c Department of Sustainable Systems Engineering (INATECH), University of Freiburg, Emmy-Noether-Str. 2, 79110, Freiburg, Germany

^d Department of Physics, University of Konstanz, 78457, Konstanz, Germany

ARTICLE INFO

Keywords:

TOPCon
Hydrogen
Atom probe tomography
Interface
Silicon solar cells

ABSTRACT

Passivated contact cell architectures have the potential for higher efficiencies than the currently dominant PERC technology. Further development requires greater understanding of the passivation mechanism and potential surface related degradation, especially at polysilicon-oxide-crystalline silicon contacts. In particular, the hydrogenation provided by high temperature firing of dielectrics has been shown to govern both initial passivation and subsequent degradation at this interface. Given the nanoscale dimensions of the tunnelling oxide, assessing the concentration of hydrogen at the interface is a complex task. In this work we use atom probe tomography to demonstrate the capacity to resolve hydrogen atoms at this interface. Atom probe tomography can provide improved depth resolution via 3D reconstructions of the elemental atomic distributions at the interface. We propose a route towards atomic scale measurements of hydrogen across a thin tunnelling oxide, which can enable further understanding of charge carrier flow at or near this interface. We show that the ability to characterise hydrogen at the nanoscale is crucially limited by the residual gas present during the atom probe measurement. Therefore deuterium, as a surrogate for naturally abundant hydrogen, is recommended to accurately provide less ambiguous determination of hydrogen concentrations at the atom scale in such structures. However, even with the use of deuterium challenges remain, and the analysis and interpretation of the data must be undertaken with care. Such atom scale characterisation can provide critical information on the role that hydrogen plays in passivating contact interfaces.

1. Introduction

Polycrystalline silicon on thin SiO_x has been shown to provide excellent behaviour as a passivating contact in silicon solar cells. Such structure has been dubbed tunnelling oxide passivating contact (TOPCon) [1] or polysilicon on oxide (POLO) [2,3]. This architecture consists of a highly doped polysilicon layer for high carrier selectivity, and an ultra-thin oxide which simultaneously provides interface passivation and sufficient majority carrier transport [1,4]. The contact can be achieved with interfacial oxide layers in the range of 1–3 nm [5], whereby the current transport occurs via tunnelling and pinhole point contact mechanisms [6]. Compared to the current industrial mainstream passivated emitter and rear cell (PERC) structure, TOPCon further

reduces contact recombination because it uses a true full area surface passivation scheme rather than localised metallisation and doping [1,7]. This design has achieved an efficiency of >26% in a small area device [5] and >24.5% for cells manufactured in an industrial environment [8]. Substantial work is currently ongoing to optimise and develop processing that enables integration of this cell architecture into high-throughput industrial production [9–11]. TOPCon is already demonstrated as a highly feasible rear design with compatibility to the existing deposition and metallisation routes. As a result, production of TOPCon cells over the past two years has increased considerably and it is in line to become a mainstream technology in the near future [12].

One of the main advantages of the TOPCon approach is the excellent passivation on the rear surface due to the combination of the thin

* Corresponding author.

E-mail address: sebastian.bonilla@materials.ox.ac.uk (R.S. Bonilla).

<https://doi.org/10.1016/j.solmat.2022.111915>

Received 15 May 2022; Received in revised form 30 June 2022; Accepted 18 July 2022

Available online 3 August 2022

0927-0248/© 2022 The Authors. Published by Elsevier B.V. This is an open access article under the CC BY license (<http://creativecommons.org/licenses/by/4.0/>).

interfacial oxide and heavily doped poly-Si layer. A critical part of the passivation is related to the hydrogenation treatment. In a TOPCon structure, the source of hydrogen is provided by a hydrogen-containing dielectric layer deposited on top of the n^+ doped poly Si [13]. A $\text{SiN}_x\text{:H}$ thin film deposited with plasma enhanced chemical deposition (PECVD) has become the most common hydrogenation choice for TOPCon structures. This $\text{SiN}_x\text{:H}$ coating has become ubiquitous within industrial silicon solar cells as its stoichiometry is tuneable in PECVD, allowing for variations in refractive index, film density and resistivity, and very importantly its hydrogen content. PECVD SiN_x is typically optimised to provide suitable dielectric optical properties and excellent surface passivation. Atomic hydrogen from this layer is released during contact firing, which can reduce the concentration of electrically active defect states at the interfacial oxide [14] and likely also within the poly-Si layer [15], which effectively suppresses minority carrier recombination. The high temperature firing step is essential in redistributing the hydrogen through the layers in the passivated contact. Despite the many advantages of TOPCon structures, several studies have recently reported a firing-induced degradation of its surface passivation [16–19]. This degradation mode has led to a five-fold increase in surface recombination currents (J_{0s}) and is solely attributed to a deterioration of surface passivation [20]. Studies found a relation between excess H content at the SiO_x interface and deterioration of passivation in n-type TOPCon [21,22]. This means that the firing step for contact formation could result in increased concentration of atomic hydrogen at/near the interfacial SiO_x , which can either (i) substantially improve surface passivation or (ii) cause severe surface related degradation, depending on the amount of hydrogen diffusion. As such, improved characterisation of the distribution of hydrogen throughout the passivated contact is critical to achieve a complete understanding of charge carrier flow at this interface, then leading to further optimization in TOPCon solar cells.

Detection of H can be achieved indirectly via electrical characterisation, where the interaction of H with active dopants or defects is measured [13]. H bonding and H complexes can be detected using deep-level transient spectroscopy (DLTS) [23], infrared spectroscopy [24], or electron paramagnetic resonance (EPR) [25], yet these methods rely on assumptions relating to H interaction. There are two main methods for identifying H chemically: mass-spectrometry based detection using Secondary Ion Mass Spectrometry (SIMS) methods [14,15,26,27], or atom probe tomography (APT) [28–30]. Both SIMS and APT can be used to analyse compositions with high sensitivity and both utilise mass spectrometers for identifying the ionic species originating from the sample. However, SIMS relies on a primary ion beam to bombard the sample surface and stimulate the emission of secondary ions. This sputtering process is known to cause atomic displacements that can result in the modification of the local composition from the drive-in effect by which primary ion bombardment implants species from the surface layer deeper into the sample, and an apparent shift or broadening appears on the detected species towards deeper into the substrate [28,31]. This type of artefact can occur for a variety of primary ion types and substrate types for any sufficiently energetic impacting beam [32]. In APT, surface atoms are ionised and field evaporated from the apex of the prepared needle-shaped sample without surface bombardment. Instead, the field evaporation process in APT for low conductivity samples like semiconductors is activated by a high-frequency pulsed laser combined with a standing electric field. A time-of-flight mass spectrometer is used for chemical identification of the evaporated ions. The spatial information associated with the detection events is recorded by a position sensitive detector, thus allowing reverse-projecting them to their original positions for a 3D reconstruction atom-by-atom map of the original sample [33]. APT can provide atomic level resolution compared to the in-depth resolution of typically on the nanometre range for SIMS, making it attractive for ultrathin structures like TOPCon.

Both SIMS and APT are vacuum based techniques, hence they inevitably suffer from a remnant concentration of H background in the experimental chamber. This makes the accurate assessment of the

hydrogen distribution in specimens very difficult since it is not possible to evacuate all residual H. This brings about large uncertainty in accurately assigning detection events as originating from the H in the sample, versus that in the vacuum chamber background. The detection limit for H in SIMS is near 10^{18} atom/ cm^3 after adjustment of vacuum and sputtering rate conditions [34,35]. In APT, the uncertainty may be higher due to contaminant hydrogen arriving at the sample, which is held at cryogenic temperatures during the experiment, possibly obfuscating hydrogen that originates from the sample itself [28,36–38]. During the APT experiment, hydrogen can evaporate in the form of H^+ , H_2^+ , H_3^+ as well as in more complex ions with other elements from the specimen, such as SiH^+ . Depending on the electric field, post-ionisation and eventual molecular dissociation may occur [37]. Since relying purely on the detection of ^1H -related signals in APT is highly inaccurate, a way to improve detectability and avoid erroneous signal is the use of isotopic marking by deuterium (D or ^2H) to distinguish between environmental hydrogen and the deuterium content from the sample [39,40]. Previous APT studies on deuterium at Si crystal defects suggest that D atoms chemically bonded at Si defects remain in the specimen during sample preparation at room temperature [30,41]. This is thanks to the milling process and conditions as will be described in Section 2. It is hence assumed that out-diffusion of trapped D is unlikely to take place during specimen preparation by ion milling in the Si structures in this work. Examples of works on investigating D charged passivation layers can already be found using SIMS in Refs. [27,42] and using APT [28].

In this work, we use TOPCon samples specially processed using deuterated silicon nitride films which can enable atom probe investigations of the distribution of ^2H across interfaces, with the further aim of correlating the H at the interface with the quality of passivation. Herein, we highlight some of the difficulties in achieving accurate deuterium distribution profiles in TOPCon structures. In particular, we highlight the importance of peak deconvolution to solve peak overlaps for complex ions formed under the laser mode. By comparing our APT results with SIMS on the same TOPCon structure, we identify artefacts that can be observed in SIMS measurements obtained in equivalent specimens.

2. Experimental methodology

In this study the examined sample consists of an untextured symmetrical n-TOPCon structure. Fig. 1 describes the layers in this structure and indicates the position from which an APT sample was obtained. The substrate is a shiny etched 200 mm n-type float zone (FZ) wafer with 10 Ω cm base resistivity. The interfacial oxide layer was grown thermally at 600 $^\circ\text{C}$ in O_2 atmosphere to ~ 1.3 nm. A 50 nm in-situ doped amorphous Si was deposited by PECVD and further crystallized at 900 $^\circ\text{C}$ for 10 min under nitrogen atmosphere to form the polysilicon layer in Fig. 1. The ~ 70 nm capping $\text{SiN}_x\text{:H}$ layer was also PECVD deposited with silane and

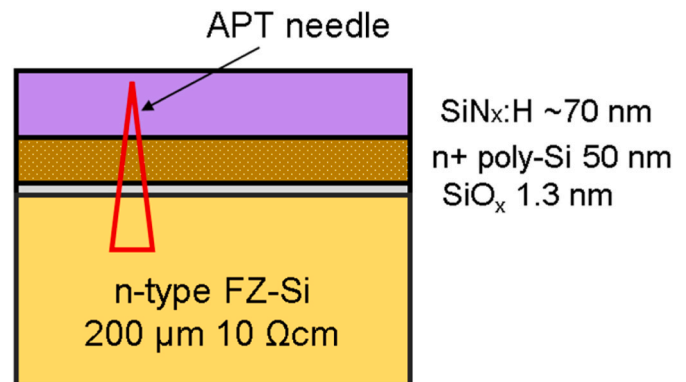


Fig. 1. Schematic of the structure of symmetrical n-TOPCon sample under investigation, one side.

deuterated ammonia as gas precursors. It should be noted that deuterium was introduced by the deuterated ammonia ND_3 gas with high isotopic enrichment. H atoms in silane SiH_4 were not replaced with D, which resulted in a SiN_xH film with partial D substitution. The sample was subsequently hot plate annealed at 500°C for 2 min for sufficient hydrogen to release and migrate into the underlying layers [17].

APT specimens containing the layered structure were prepared from the TOPCon samples using a Zeiss NVision 40 FIB-SEM via the in-situ lift-out process described in Ref. [43]. The surface of the TOPCon samples was preserved using a >500 nm tungsten layer which was ion-beam deposited in-situ before tip sharpening, in the NVision using a Zeiss gas injection system. This protects the underlying layers from Ga^+ ion beam damage during subsequent milling. Fig. 2 (a) shows the brighter tungsten layer on top of the TOPCon layers when the specimen is undergoing needle sharpening. The tungsten layer was subsequently completely removed during the final sharpening steps and the final APT specimen takes the shape of a needle with a radius <100 nm. A final polishing with a low energy 2 kV gallium beam was carried out to remove any Ga^+ damage during sharpening. Fig. 2 (b) shows a representative final APT specimen after the sharpening and polishing.

Atomic scale chemical analysis of the specimen was performed using a CAMECA local electrode atom probe (LEAP) 5000 XR with a 52% detection efficiency. The atom probe specimens were run at a temperature of 50 K, a pulse frequency of 200 kHz, and a moderate target detection rate of 1.0%. The CAMECA AP Suite 6.1 software was used to produce the reconstruction. Compositional analyses were conducted using AtomProbeLab (v.0.2.4) and a minimum isotopic abundance of 0.04% to exclude naturally occurring deuterium from the analysis. The APT reconstruction follows the voltage curve to estimate the radius evolution of the specimen. Because the structure consists of a stack of dielectric and semiconductors, laser pulse mode is the viable choice over voltage mode to prevent premature fracture under high fields. Note that laser pulse evaporation leads to enhanced complex ion formation and peak overlaps in the mass-spectrum, which adds complexity to the identification of D content in the specimen. A range of UV laser energies from 10 to 70 pJ were initially tested using a blank Si needle specimen before the TOPCon specimens were run. An optimal running condition was set to be 60 pJ for the TOPCon samples.

3. Results and discussion

3.1. Effect of laser energy on H background

One of the critical experimental factors influencing the detected hydrogen background in APT is the laser pulse energy. A laser energy test was initially carried out on a lowly doped Si specimen without any

processing, and hence with effectively zero built-in H concentration. Representative conditions of 50 K base temperature, 200 kHz laser pulse frequency and a target detection rate of 1.4% were used. Fig. 3 (a) shows the impact of variations in laser energy on the measured hydrogen and silicon content, respectively, where all the detected H originates from environmental background. Plotted on the primary y-axis in Fig. 3 (a) is the ratio between atomic and molecular hydrogen counts at mass-to-charge-state ratios of 1 Da and 2 Da, and total ^{28}Si counts at 14 Da and 28 Da. This is chosen as a representative of the H background level. It is shown that detected background H peaks at intermediate laser energies around 30 pJ and drops at both high and low laser energies. It is also clear that a significant reduction of background content can be achieved with higher energy pulses over 50 pJ. Such an effect of laser energy on the detected H level has been observed and discussed in other works [37,38]. It is most likely that the intensity of the applied electric field significantly influences the observed results. With the application of higher laser energy, to maintain the same evaporation rate (i.e. ions detected per laser pulse) the DC electric field strength at the evaporating tip decreases. Such a decreasing surface field is tracked by the decreasing Si relative charge state ratio (Si^+ to Si^{2+}) as shown on the secondary y-axes scale in Fig. 3 (a). Under such decreasing field conditions, the absorption of background hydrogen to the specimen is reduced resulting in the reduced detection of background H. This preliminary characterisation indicates that high laser energies are advantageous for keeping background H noise low.

The \log_{10} of the H_2^+ to H^+ ratio is plotted against laser energy in Fig. 3 (b). This plot shows a shift from atomic H^+ to molecular H_2^+ under high laser energy and low field conditions. The reason is that the post evaporation process of molecular dissociation into atomic H is dependent on near-surface field strength and it is hence suppressed at low field conditions [37]. The shift to more H_2^+ , however, is disadvantageous in specimens with introduced D. $^1\text{H}_2^+$ overlaps with the $^2\text{D}^+$ signal at 2 Da on the mass spectrum, which adds large uncertainty in interpreting the deuterium signals. There is a trade-off between lowering overall background H and its increased detection of $^1\text{H}_2^+$ when using higher laser energies, hence a laser energy of 60 pJ is chosen as the running condition for the APT of TOPCon samples containing deuterium.

3.2. 3D atomic scale reconstructions of the TOPCon structure

Fig. 4 shows a set of 3D reconstructed atom maps produced by APT for the TOPCon sample displayed schematically in Fig. 2. The different layers in the structure are labelled in the figure including the crystalline silicon wafer, the thin tunnel SiO_x layer, the n^+ doped polysilicon layer, and the capping SiN_xH dielectric. Each of the five maps shown in Fig. 4 focus on a different ionic species, identified from a specific mass-to-

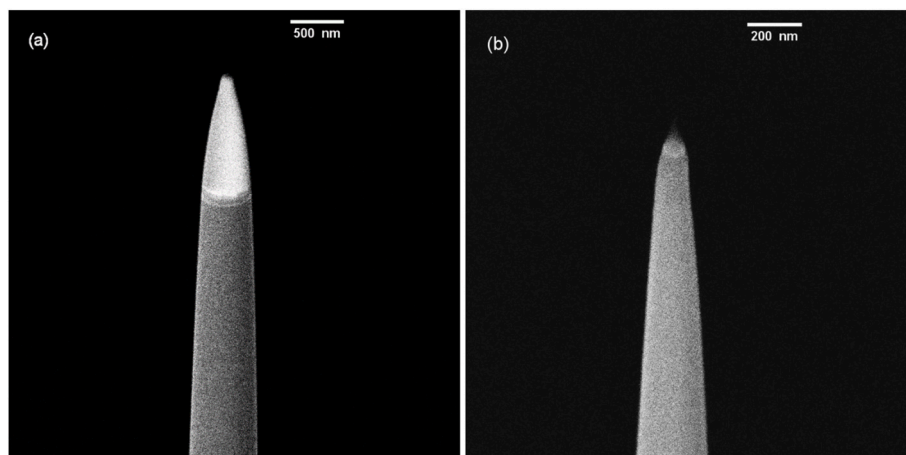


Fig. 2. SEM images of (a) APT specimen before final sharpening, and (b) a finished APT needle specimen. Note the different size scales.

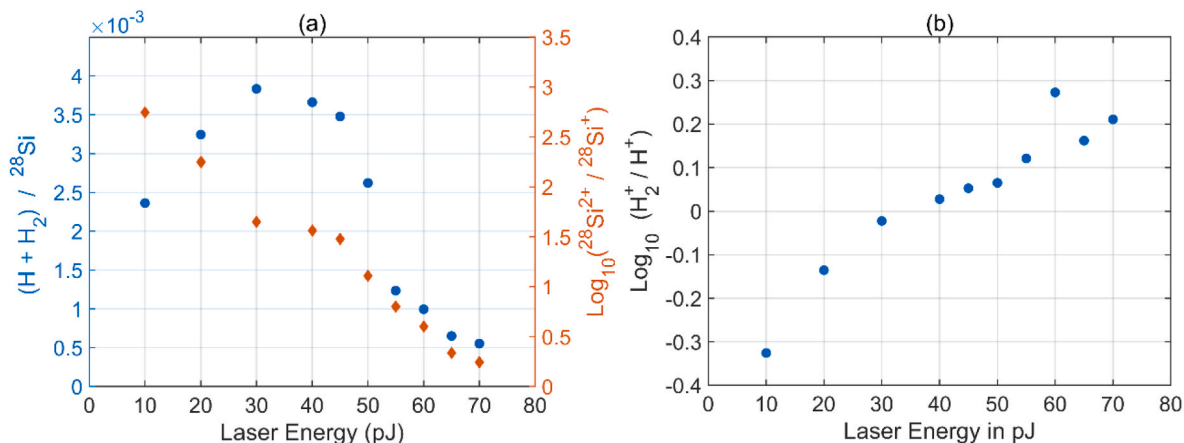


Fig. 3. Ratios of APT detected species from a pure Si specimen as a function of laser pulse energy. (a) Left scale: Ratio of H counts at 1 Da and 2 Da to total ${}^{28}\text{Si}$ counts at 14 Da and 28 Da, right scale: Log ratio of ${}^{28}\text{Si}^{2+}$ at 14 Da to ${}^{28}\text{Si}^+$ at 28 Da, both plotted against laser pulse energy. (b) Log ratio of H_2^+ to H^+ plotted against laser pulse energy. 1 Da (Da) is equivalent to a mass-to-charge-state ratio of 1.

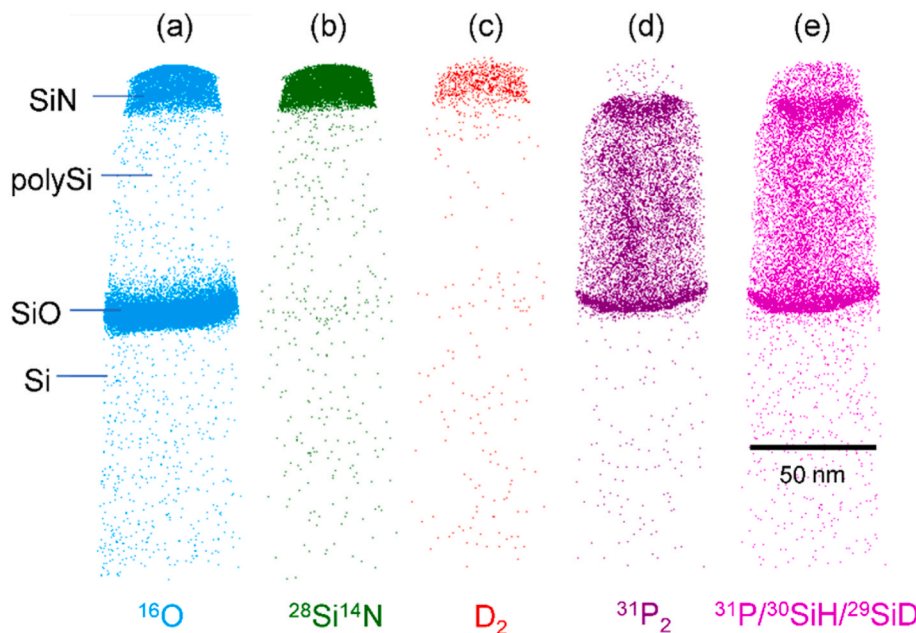


Fig. 4. 3D atom maps of the TOPCon structure for relevant species: (a) ${}^{16}\text{O}^+$ (b) ${}^{28}\text{Si}^{14}\text{N}^+$ (c) D_2^+ (d) ${}^{31}\text{P}_2^+$ (e) ${}^{31}\text{P}^+$ or ${}^{30}\text{SiH}^+$ or ${}^{29}\text{SiD}^+$ at 31 Da.

charge-state ratio in the mass spectrum. The mass-spectrum for the specimen is presented in the supporting information Fig. S1. Fig. 4 (a) represents the oxygen signal using only the 16 Da O^+ signal, where two regions featuring an accumulation of oxygen are evident. The first peak is located in the interfacial SiO_x layer, which is to be expected and serves as a spatial marker for the tunnelling oxide. The second high concentration of O occurs in the SiN_x layer. This O can originate from oxidation occurring during the PECVD and hotplate annealing processes.

Fig. 4 (b) represents the signal for nitrogen obtained using the 42 Da signal, which represents the mass-to-charge-state ratio for the SiN^+ complex ion. The atomic mass number for atomic nitrogen is 14. However, the peak on the mass-to-charge-state-ratio spectrum at 14 Da represents an overlap of signals from ${}^{28}\text{Si}^{2+}$ and ${}^{14}\text{N}^+$ ions. Hence, the SiN^+ complex ion is chosen here as more fitting to demonstrate the N distribution and define the location of the SiN_x layer. Fig. 4 (c) represents the distribution of ions with a mass-to-charge-state ratio of 4 Da. As discussed, the background hydrogen noise from the chamber occurs at either 1 Da for atomic H^+ , or 2 Da for molecular H_2^+ . At a mass-to-charge-state ratio of 4 Da there is no signal related to background hydrogen

adding noise to the detection. Therefore, this signal allows unambiguous detection of hydrogen as a ${}^2\text{D}_2^+$ species. Unfortunately, the signal detected for ${}^2\text{D}_2^+$ in this sample is weak. We can observe a concentration of ${}^2\text{D}_2^+$ in the SiN_x layer as expected since it served as the deuterium source, however, ${}^2\text{D}_2^+$ is not detected significantly at the c-Si/ SiO_x interface.

The species shown in Fig. 4 (d) has a mass-to-charge-state ratio of 62 Da. The atomic mass of phosphorous is 31. Besides ${}^{31}\text{P}_2^+$, based upon analysis of all the peaks in the spectrum, other complex ions at 62 Da would be highly unlikely and hence this signal is attributed solely to the presence of phosphorous. As shown, phosphorous is found in the n + doped polysilicon layer. Interestingly, we observe an accumulation of P at both interfaces of the doped poly Si layer as has also been reported in other work [44]. This can be explained by P segregation to the interfaces during the 900 °C annealing for crystallisation of the poly-Si layer.

Finally, Fig. 4 (e) represents a mass-to-charge-state ratio of 31. Phosphorous has an atomic mass of 31 and hence this signal is dominated by ${}^{31}\text{P}^+$. This explains the similar profile to Fig. 4 (d). However, this mass peak contains an overlap with a silicon-hydrogen complex ion

peak. Both $^{30}\text{Si}^+\text{H}^+$ and $^{29}\text{Si}^+\text{D}^+$ can contribute to this signal. Thus, the difference in the atomic map between Fig. 4 (d) and (e) is likely in part related to presence of D or H in the structure. This could explain the additional component of signal at 31 Da which can be observed in the SiN_x layer in Fig. 4 (e). The overlap at 31 Da prevents seeing the true distributions of each of the species from the atom map in Fig. 4 (e). This highlights the importance of peak deconvolution in the accurate depiction of chemical profiles in APT [40,45].

3.3. Depths profiles of elements

The previous section identified the presence of various peak overlaps on the mass spectra recorded, which can lead to incorrect interpretation of the APT data. To address these overlaps, using knowledge of natural isotopic abundances of elements and analysis of neighbouring peaks, the peak overlap solving procedure proposed in Ref. [45] can be applied to estimate the relative contributions of the overlapping ionic species to the intensity of the peak. The method devised by London et al. was used to solve peak overlaps, using the maximum likelihood estimation (MLE) [46]. An example of a solved overlap group at 28–32 Da is given in a histogram in the supporting information Fig. S2. Such a peak solving protocol is applied by splitting the sample into a number of bins along the depth direction, to find the mean local compositions as a function of depth into the specimen, using 1 nm width bins. The composition profiles for different elements after the decomposition is given in Fig. 5.

The oxygen composition profile is given in the blue curve in Fig. 5 and is used to locate different layers as marked on the top side. It is noted that due to some simplifying assumptions that underpin the APT reconstruction algorithm, the resulting reconstruction do not give perfectly flat interfaces perpendicular to axes of the needle specimen, i. e. the depth direction in Fig. 5. Due to this, an artefact for the element profiles picture in Fig. 5 is the apparent widening of the oxide layer and spread-out of species at the interface. Supporting information Fig. S3 provides an explanation of such phenomenon. Additionally, compositional discontinuity can induce ion trajectory aberrations that distort the projected 3D image [47,48], which can also limit the accuracy when measuring spatially the oxide layer width. Correlated microscopy with TEM is needed to calibrate the compositional data against the structural information and provide accurate oxide layer thickness. This will be pursued in future work.

The P profile shows accumulation at both ends of poly-Si as expected from the 3D reconstruction in Fig. 4. Interestingly, from the semi-

logarithmic plot Fig. S4 (b), P concentration falls sharply over 2 orders of magnitude within a 10 nm length scale into the c-Si. This points to very little P penetration locally within our APT sample. We here provide evidence that P in-diffusion is minimum under current processing scheme, in contrast to observations via SIMS.

Because both H_2^+ and D^+ are the only species present in the peak at 2 Da, this peak is unsolvable as there is not sufficient information to distinguish them. To overcome this, we have created two D profiles indicating (i) an upper bound of D when the 2 Da peak counts is assigned to D^+ in the specimen, and (ii) a lower bound of D when 2 Da is assigned to H_2^+ with all D content in this case coming from complex ions involving D. The real concentration of D in this sample lies between these bounds. In agreement with the observations for 3D reconstructions, it is shown here that the depth profile of D has highest concentration in SiN_x . A small build-up of D to a level of 0.38 at% ($\sim 10^{20} \text{ cm}^{-3}$) is seen at the oxide layer at the lower D bond.

SIMS depth profiles for an equivalent specimen are included in the supporting information Fig. S4 (a), alongside the comparable APT profiles in S4 (b). The sharp fall of P and O concentrations beyond the interface in the APT profiles goes in conflict with the extended tails in the SIMS profiles. This can be evidence that extended tails of the species in SIMS are largely due to a known SIMS artefact resulting from primary beam bombardment that pushes atoms inwards. This points out to the need of improving SIMS data interpretation for chemical detection of dopants when studying the dopant penetration and hydrogenation for TOPCon structures.

4. Conclusion

Accurate analysis of the distribution of hydrogen throughout a TOPCon passivated contact is critical for understanding surface passivation and degradation. In this paper, we use atom probe tomography to understand the role of hydrogen in TOPCon passivation schemes consisting of a thin tunnel oxide and doped poly silicon layers. APT can provide 3D atomic mapping of elements, however, the residual H present in the chamber during the measurement can have a large detrimental impact on the accuracy of the mapping. This presents a challenge in understanding the role of hydrogen in surface passivation. We show that the choice of laser energy in the APT experiment has a large impact on the amount of background hydrogen in the image. Herein, we provide volumetric reconstructions of atomic species detected in TOPCon samples, using deuterium as a marker for hydrogen. The 3D atomic maps were then deconvoluted to produce depth profiles of D, O and P in a TOPCon structure. A small build-up of deuterium was identified with a concentration of at least 0.38 at% at the interface between the oxide layer and crystalline silicon. By comparing this with SIMS depth profiles for the same TOPCon structure, we provide evidence that the long penetration tails of D and P commonly observed in SIMS can be due to experimental artefacts. This can impact the analysis of hydrogen distribution at the interface. Understanding the atom distribution with APT is a critical step for future development and optimization of passivated contacts in high efficiency silicon solar cells.

CRediT authorship contribution statement

Yifu Shi: Writing – review & editing, Writing – original draft, Visualization, Investigation, Formal analysis, Data curation. **Megan E. Jones:** Writing – review & editing, Visualization, Methodology, Formal analysis. **Martin S. Meier:** Writing – review & editing, Methodology, Investigation, Data curation. **Matthew Wright:** Writing – review & editing, Writing – original draft, Supervision. **Jana-Isabelle Polzin:** Writing – review & editing, Resources, Investigation. **Wolfram Kwapil:** Writing – review & editing, Resources, Investigation. **Christian Fischer:** Investigation. **Martin C. Schubert:** Writing – review & editing, Supervision, Resources, Funding acquisition. **Chris Grovenor:** Writing – review & editing, Supervision. **Michael Moody:** Writing – review &

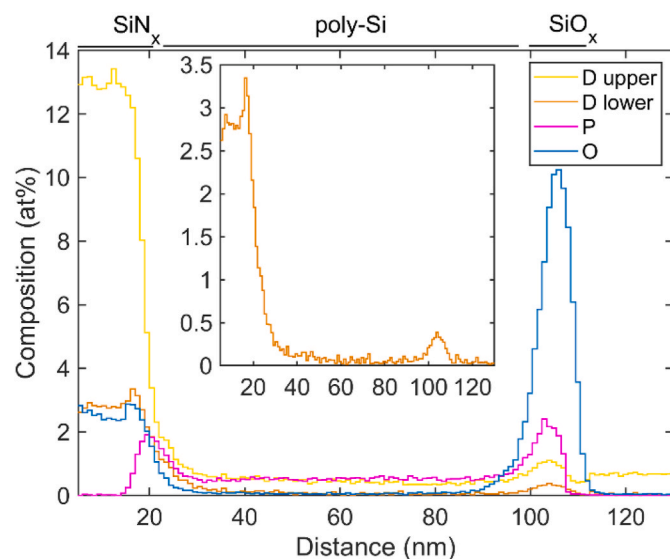


Fig. 5. Depth profiles of deuterium, phosphorous and oxygen obtained from APT data analysis.

editing, Supervision, Project administration, Funding acquisition, Conceptualization. **Ruy S. Bonilla:** Writing – review & editing, Supervision, Resources, Project administration, Funding acquisition, Conceptualization.

Declaration of competing interest

The authors declare that they have no known competing financial interests or personal relationships that could have appeared to influence the work reported in this paper.

Data availability

All data created during this research and published in this article is openly available from the Oxford University Research Archive and can be downloaded free of charge from <http://ora.ox.ac.uk>.

Acknowledgements

Y. Shi would like to thank the China Scholarship Council for funding his studies. M. E. Jones acknowledges funding from EPSRC, National Nuclear Laboratory and Rolls Royce plc. M. Schubert, W. Kwapil and J. Polzin acknowledge the support from the German Federal Ministry for Economic Affairs and Energy (BMW) within the research projects Hydra under grants 03EE1052B and 03EE1052D. C. Fischer acknowledge the support from Hydra grant 03EE1052A. This work was supported by the UK Engineering and Physical Sciences Research Council grant number EP/V038605/1 and EP/S021663/1. R.S. Bonilla was supported by the Royal Academy of Engineering under the Research Fellowship scheme.

Appendix A. Supplementary data

Supplementary data to this article can be found online at <https://doi.org/10.1016/j.solmat.2022.111915>.

References

- [1] F. Feldmann, M. Bivour, C. Reichel, H. Steinkemper, M. Hermle, S.W. Glunz, Tunnel oxide passivated contacts as an alternative to partial rear contacts, *Sol. Energy Mater. Sol. Cells* 131 (2014) 46–50, <https://doi.org/10.1016/j.solmat.2014.06.015>.
- [2] M. Rienacker, M. Bossmeyer, A. Merkle, U. Römer, F. Haase, J. Krügener, R. Brendel, R. Peibst, Junction resistivity of carrier-selective polysilicon on oxide junctions and its impact on solar cell performance, *IEEE J. Photovoltaics* 7 (2017) 11–18, <https://doi.org/10.1109/JPHOTOV.2016.2614123>.
- [3] U. Römer, R. Peibst, T. Ohndes, B. Lim, J. Krügener, T. Wietler, R. Brendel, Ion implantation for poly-Si passivated back-junction back-contacted solar cells, *IEEE J. Photovoltaics* 5 (2015) 507–514, <https://doi.org/10.1109/JPHOTOV.2014.2382975>.
- [4] S.W. Glunz, B. Steinhäuser, J.I. Polzin, C. Luderer, B. Grübel, T. Niewelt, A.M.O. M. Okasha, M. Bories, H. Nagel, K. Krieg, F. Feldmann, A. Richter, M. Bivour, M. Hermle, Silicon-based passivating contacts: the TOPCon route, *Prog. Photovoltaics Res. Appl.* (2021), <https://doi.org/10.1002/PIP.3522>.
- [5] F. Haase, C. Hollemann, S. Schäfer, A. Merkle, M. Rienacker, J. Krügener, R. Brendel, R. Peibst, Laser contact openings for local poly-Si-metal contacts enabling 26.1%-efficient POLO-IBC solar cells, *Sol. Energy Mater. Sol. Cells* 186 (2018) 184–193, <https://doi.org/10.1016/j.solmat.2018.06.020>.
- [6] R. Peibst, U. Römer, Y. Larionova, M. Rienacker, A. Merkle, N. Folchert, S. Reiter, M. Turcu, B. Min, J. Krügener, D. Tetzlaff, E. Bugiel, T. Wietler, R. Brendel, Working principle of carrier selective poly-Si/c-Si junctions: is tunnelling the whole story? *Sol. Energy Mater. Sol. Cells* 158 (2016) 60–67, <https://doi.org/10.1016/j.solmat.2016.05.045>.
- [7] J. Schmidt, R. Peibst, R. Brendel, Surface passivation of crystalline silicon solar cells: present and future, *Sol. Energy Mater. Sol. Cells* 187 (2018) 39–54, <https://doi.org/10.1016/j.solmat.2018.06.047>.
- [8] R. Chen, M. Wright, D. Chen, J. Yang, P. Zheng, X. Zhang, S. Wenham, A. Ciesla, 24.58% efficient commercial n-type silicon solar cells with hydrogenation, *Prog. Photovoltaics Res. Appl.* 29 (2021) 1213–1218, <https://doi.org/10.1002/PIP.3464>.
- [9] Y. Chen, D. Chen, C. Liu, Z. Wang, Y. Zou, Y. He, Y. Wang, L. Yuan, J. Gong, W. Lin, X. Zhang, Y. Yang, H. Shen, Z. Feng, P.P. Altermatt, P.J. Verlinden, Mass production of industrial tunnel oxide passivated contacts (i-TOPCon) silicon solar cells with average efficiency over 23% and modules over 345 W, *Prog. Photovoltaics Res. Appl.* 27 (2019) 827–834, <https://doi.org/10.1002/PIP.3180>.
- [10] Z. Liu, J. Chen, Z. Qiao, R. Liu, C. Chen, L. Ma, J. Bao, W. Wu, Development of industrial n-type bifacial TOPCon solar cells and modules, in: 36th Eur. Photovolt. Sol. Energy Conf. Exhib. 2019, pp. 100–102, <https://doi.org/10.4229/EUPVSEC20192019-2BP.1.5>.
- [11] Q. Wang, W. Wu, N. Yuan, Y. Li, Y. Zhang, J. Ding, Influence of SiO_x film thickness on electrical performance and efficiency of TOPCon solar cells, *Sol. Energy Mater. Sol. Cells* 208 (2020), 110423, <https://doi.org/10.1016/j.solmat.2020.110423>.
- [12] B. Kafle, B.S. Goraya, S. Mack, F. Feldmann, S. Nold, J. Rentsch, TOPCon – technology options for cost efficient industrial manufacturing, *Sol. Energy Mater. Sol. Cells* 227 (2021), 111100, <https://doi.org/10.1016/j.solmat.2021.111100>.
- [13] B.J. Hallam, P.G. Hamer, A.M. Ciesla née Wenham, C.E. Chan, B. Vicari Stefani, S. Wenham, Development of advanced hydrogenation processes for silicon solar cells via an improved understanding of the behaviour of hydrogen in silicon, *Prog. Photovoltaics Res. Appl.* 28 (2020) 1217–1238, <https://doi.org/10.1002/PIP.3240>.
- [14] M. Schnabel, B.W.H. van de Loo, W. Nemeth, B. Maccio, P. Stradins, W.M. M. Kessels, D.L. Young, Hydrogen passivation of poly-Si/SiO_x contacts for Si solar cells using Al₂O₃ studied with deuterium, *Appl. Phys. Lett.* 112 (2018), 203901, <https://doi.org/10.1063/1.5031118>.
- [15] T.N. Truong, D. Yan, W. Chen, M. Tebyetekerwa, M. Young, M. Al-Jassim, A. Cuevas, D. Macdonald, H.T. Nguyen, Hydrogenation mechanisms of poly-Si/SiO_x passivating contacts by different capping layers, *Sol. RRL* 4 (2020), <https://doi.org/10.1002/SOLR.201900476>.
- [16] M. Winter, S. Bordin, R. Peibst, R. Brendel, J. Schmidt, Degradation and regeneration of n+-doped poly-Si surface passivation on p-type and n-type cz-Si under illumination and dark annealing, *IEEE J. Photovoltaics* 10 (2020) 423–430, <https://doi.org/10.1109/JPHOTOV.2020.2964987>.
- [17] J.I. Polzin, B. Hammann, T. Niewelt, W. Kwapil, M. Hermle, F. Feldmann, Thermal activation of hydrogen for defect passivation in poly-Si based passivating contacts, *Sol. Energy Mater. Sol. Cells* 230 (2021), 111267, <https://doi.org/10.1016/j.solmat.2021.111267>.
- [18] D. Kang, H.C. Sio, D. Yan, J. Stuckelberger, X. Zhang, D. Macdonald, Firing stability of phosphorus-doped polysilicon passivating contacts: factors affecting the degradation behavior, *Sol. Energy Mater. Sol. Cells* 234 (2022), 111407, <https://doi.org/10.1016/j.solmat.2021.111407>.
- [19] D. Chen, C. Madumelu, M. Kim, B.V. Stefani, A. Soeriyadi, D. Kang, H.C. Sio, X. Zhang, P. Zhu, B. Hallam, M. Wright, Investigating the degradation behaviours of n+-doped Poly-Si passivation layers: an outlook on long-term stability and accelerated recovery, *Sol. Energy Mater. Sol. Cells* 236 (2022), 111491, <https://doi.org/10.1016/j.solmat.2021.111491>.
- [20] D. Kang, H.C. Sio, D. Yan, W. Chen, J. Yang, J. Jin, X. Zhang, D. Macdonald, Long-term stability study of the passivation quality of polysilicon-based passivation layers for silicon solar cells, *Sol. Energy Mater. Sol. Cells* 215 (2020), 110691, <https://doi.org/10.1016/j.solmat.2020.110691>.
- [21] D. Kang, H.C. Sio, J. Stuckelberger, R. Liu, D. Yan, X. Zhang, D. Macdonald, Optimum hydrogen injection in phosphorus-doped polysilicon passivating contacts, *ACS Appl. Mater. Interfaces* 13 (2021) 55164–55171, https://doi.org/10.1021/ACSAMI.1C17342/ASSET/IMAGES/ACSAMI.1C17342.SOCIAL.JPEG_V03.
- [22] C. Hollemann, N. Folchert, S.P. Harvey, P. Stradins, D.L. Young, C. Lima, S. De Souza, M. Rienacker, F. Haase, R. Brendel, R. Peibst, Changes in hydrogen concentration and defect state density at the poly-Si/SiO_x/c-Si interface due to firing, <https://doi.org/10.1016/j.solmat.2021.111297>, 2021.
- [23] K. Bonde-Nielsen, B. Bech-Nielsen, J. Hansen, E. Andersen, J.U. Andersen, Bond-centered hydrogen in silicon studied by in situ deep-level transient spectroscopy, *Phys. Rev. B Condens. Matter* 60 (1999) 1716–1728, <https://doi.org/10.1103/PHYSREVB.60.1716>.
- [24] C. Vargas, K. Kim, G. Coletti, D. Payne, C. Chan, S. Wenham, Z. Hameiri, Carrier-induced degradation in multicrystalline silicon: dependence on the silicon nitride passivation layer and hydrogen released during firing, *IEEE J. Photovoltaics* 8 (2018) 413–420, <https://doi.org/10.1109/JPHOTOV.2017.2783851>.
- [25] P. Stallings, P. Johannesen, S. Herström, K. Bonde Nielsen, B. Bech Nielsen, J. Byberg, Electron paramagnetic resonance study of hydrogen-vacancy defects in crystalline silicon, *Phys. Rev. B Condens. Matter* 58 (1998) 3842–3852, <https://doi.org/10.1103/PHYSREVB.58.3842>.
- [26] D. Kang, H.C. Sio, D. Yan, J. Stuckelberger, X. Zhang, D. Macdonald, Firing stability of phosphorus-doped polysilicon passivating contacts: factors affecting the degradation behavior, *Sol. Energy Mater. Sol. Cells* 234 (2022), <https://doi.org/10.1016/j.solmat.2021.111407>.
- [27] M. Lehmann, N. Valle, J. Horzel, A. Pshenova, P. Wyss, M. Döbeli, M. Despeisse, S. Eswara, T. Wirtz, Q. Jeangros, A. Hessler-Wyser, F.J. Haug, A. Ingenito, C. Ballif, Analysis of hydrogen distribution and migration in fired passivating contacts (FPC), *Sol. Energy Mater. Sol. Cells* 200 (2019), 110018, <https://doi.org/10.1016/j.solmat.2019.110018>.
- [28] S. Pal, J. Barrirero, M. Lehmann, Q. Jeangros, N. Valle, F.J. Haug, A. Hessler-Wyser, C.N. Shyam Kumar, F. Mücklich, T. Wirtz, S. Eswara, Quantification of hydrogen in nanostructured hydrogenated passivating contacts for silicon photovoltaics combining SIMS-APT-TEM: a multiscale correlative approach, *Appl. Surf. Sci.* 555 (2021), 149650, <https://doi.org/10.1016/j.apsusc.2021.149650>.
- [29] H. Park, S. Bae, S.J. Park, J.Y. Hyun, C.H. Lee, D. Choi, D. Kang, H. Han, Y. Kang, H.S. Lee, D. Kim, Role of polysilicon in poly-Si/SiO_x passivating contacts for high-efficiency silicon solar cells, *RSC Adv.* 9 (2019) 23261–23266, <https://doi.org/10.1039/C9RA03560E>.
- [30] D. Tweddle, P. Hamer, Z. Shen, V.P. Markevich, M.P. Moody, P.R. Wilshaw, Direct observation of hydrogen at defects in multicrystalline silicon, *Prog. Photovoltaics Res. Appl.* (2019) 3184, <https://doi.org/10.1002/PIP.3184>, pip.

- [31] M. Cwil, P. Konarski, J. Ciosek, Ion mass interferences and matrix effects on SIMS depth profiling of thin Ti/Si multilayer films induced by hydrogen, carbon and oxygen contaminations, *Int. J. Mass Spectrom.* 263 (2007) 54–58, <https://doi.org/10.1016/j.jms.2006.12.004>.
- [32] P. Van der Heide, Secondary ion mass spectrometry: an introduction to principles and practices. https://books.google.com/books?hl=zh-CN&lr=&id=4xdVBAAQBAJ&oi=fnd&pg=PT9&dq=secondary+ion+mass+spectrometry&ots=3kk0LMUZfP&sig=8At67ID_3ceglHnSFSKgVQ3GWz0, 2014. (Accessed 24 April 2022).
- [33] B. Gault, *Atom Probe Microscopy*, 2012.
- [34] K. Wittmaack, Background formation in SIMS analysis of hydrogen, carbon, nitrogen and oxygen in silicon, *Nucl. Instrum. Methods Phys. Res.* 218 (1983) 327–332, [https://doi.org/10.1016/0167-5087\(83\)91001-3](https://doi.org/10.1016/0167-5087(83)91001-3).
- [35] F.A. Stevie, C. Zhou, M. Hopstaken, M. Saccomanno, Z. Zhang, A. Turansky, SIMS measurement of hydrogen and deuterium detection limits in silicon: comparison of different SIMS instrumentation, *J. Vac. Sci. Technol. B, Nanotechnol. Microelectron. Mater. Process. Meas. Phenom.* 34 (2016), 03H103, <https://doi.org/10.1116/1.4940151>.
- [36] Y. Kunimune, Y. Shimada, Y. Sakurai, M. Inoue, A. Nishida, B. Han, Y. Tu, H. Takamizawa, Y. Shimizu, K. Inoue, F. Yano, Y. Nagai, T. Katayama, T. Ide, Quantitative analysis of hydrogen in SiO₂/SiN/SiO₂ stacks using atom probe tomography, *AIP Adv.* 6 (2016), <https://doi.org/10.1063/1.4948558>.
- [37] G. Sundell, M. Thuvander, H.O. Andrén, Hydrogen analysis in APT: methods to control adsorption and dissociation of H₂, *Ultramicroscopy* 132 (2013) 285–289, <https://doi.org/10.1016/j.ultramic.2013.01.007>.
- [38] R.P. Kolli, Controlling residual hydrogen gas in mass spectra during pulsed laser atom probe tomography, *Adv. Struct. Chem. Imag.* 3 (2017), <https://doi.org/10.1186/S40679-017-0043-4>.
- [39] J. Takahashi, K. Kawakami, Y. Kobayashi, T. Tarui, The first direct observation of hydrogen trapping sites in TiC precipitation-hardening steel through atom probe tomography, *Scripta Mater.* 63 (2010) 261–264, <https://doi.org/10.1016/j.scriptamat.2010.03.012>.
- [40] I. Mouton, A.J. Breen, S. Wang, Y. Chang, A. Szczepaniak, P. Kontis, L. T. Stephenson, D. Raabe, M. Herbig, T. Ben Britton, B. Gault, Quantification Challenges for Atom Probe Tomography of Hydrogen and Deuterium in Zircaloy-4, Cambridge.Org, 2019, <https://doi.org/10.1017/S143192761801615X>.
- [41] H. Takamizawa, K. Hoshi, Y. Shimizu, F. Yano, K. Inoue, S. Nagata, T. Shikama, Y. Nagai, Three-dimensional characterization of deuterium implanted in silicon using atom probe tomography, *APEX* 6 (2013), 066602, <https://doi.org/10.7567/APEX.6.066602/XML>.
- [42] G. Dingemans, W. Beyer, M.C.M. Van De Sanden, W.M.M. Kessels, Hydrogen induced passivation of Si interfaces by Al₂O₃ films and SiO₂/Al₂O₃ stacks, *Appl. Phys. Lett.* 97 (2010), 152106, <https://doi.org/10.1063/1.3497014>.
- [43] K. Thompson, D. Lawrence, D.J. Larson, J.D. Olson, T.F. Kelly, B. Gorman, In situ site-specific specimen preparation for atom probe tomography, *Ultramicroscopy* 107 (2007) 131–139, <https://doi.org/10.1016/j.ultramic.2006.06.008>.
- [44] F. Feldmann, J. Schön, J. Niess, W. Lerch, M. Hermle, Studying dopant diffusion from Poly-Si passivating contacts, *Sol. Energy Mater. Sol. Cells* 200 (2019), 109978, <https://doi.org/10.1016/j.solmat.2019.109978>.
- [45] A.J. London, D. Haley, M.P. Moody, Single-ion deconvolution of mass peak overlaps for atom probe microscopy, *Microsc. Microanal.* 23 (2017) 300–306, <https://doi.org/10.1017/S1431927616012782>.
- [46] A.J. London, Quantifying uncertainty from mass-peak overlaps in atom probe microscopy, *Microsc. Microanal.* 25 (2019) 378–388, <https://doi.org/10.1017/S1431927618016276>.
- [47] B. Gault, A. Chieramonti, O. Cojocaru-Mirédin, P. Stender, R. Dubosq, C. Freysoldt, S.K. Makineni, T. Li, M. Moody, J.M. Cairney, Atom probe tomography, *Nat. Rev. Methods Prim.* 11 (1) (2021) 1–30, <https://doi.org/10.1038/s43586-021-00047-w>, 2021.
- [48] B.M. Jenkins, F. Danoix, M. Gouné, P.A.J. Bagot, Z. Peng, M.P. Moody, B. Gault, Reflections on the analysis of interfaces and grain boundaries by atom probe tomography, *Microsc. Microanal.* 26 (2020) 247–257, <https://doi.org/10.1017/S1431927620000197>.